Small Methods

small methods
www.small-methods.com

RESEARCH ARTICLE OPEN ACCESS

Guiding the Formation of Surface-Confined 2D Metal–Organic Coordination Networks by Variation of Constituent Landing Energy in Electrospray Deposition of an Iron(II) Grid Complex

Dennis Meier[1] | Benedikt Schoof[1] | Andreas Walz[1,2] | Nithin Suryadevara[3] | Annette Huettig[1,2] | Hartmut Schlichting[1,2] | Joachim Reichert[1] | Mario Ruben[3,4,5] | Anthoula C. Papageorgiou[1,6] | Johannes V. Barth[1]

[1]Physics Department E20, TUM School of Natural Sciences, Technical University of Munich, Garching, Germany | [2]pureions GmbH, Gilching, Germany | [3]Institute of Nanotechnology, Karlsruhe Institute of Technology (KIT), Eggenstein-Leopoldshafen, Germany | [4]Institute for Quantum Materials and Technologies, Karlsruhe Institute of Technology (KIT), Eggenstein-Leopoldshafen, Germany | [5]Centre Européen de Sciences Quantiques (CESQ), Institut De Science et D'ingénierie Supramoléculaires (ISIS), Strasbourg, France | [6]Laboratory of Physical Chemistry, Department of Chemistry, National and Kapodistrian University of Athens, Athens, Greece

Correspondence: Anthoula C. Papageorgiou (a.c.papageorgiou@chem.uoa.gr)

Received: 1 August 2025 | **Revised:** 29 January 2026 | **Accepted:** 29 January 2026

Keywords: electrospray ionization | ion beam deposition | metal–organic network | scanning tunneling microscopy | spin crossover complex

ABSTRACT

The combination of electrospray ionization with ion beam deposition in ultra-high vacuum has opened new opportunities to research non-sublimable molecules on solid surfaces in recent years. An Fe(II) [2 × 2] grid complex was deposited on Ag(111) and investigated by scanning tunneling microscopy. Low landing energies (< 3 eV z^{-1}) resulted in clusters and single structures with potentially intact coordination bonds. Higher landing energies (> 3 eV z^{-1}) led to coordination bond cleavage and a rich variety of self-assembled surface networks formed spontaneously by the grid fragments. Applying established on-surface synthesis methodology employing the constituents of these networks (ligands and Fe atoms) reproduced only a part of them. It is thus proposed that electrospray ion beam deposition is a different route to on-surface coordination network synthesis.

1 | Introduction

Electrospray ionization (ESI) is a gentle method used to transfer molecules from solution into the gas phase, making it an invaluable tool for mass spectrometry and other analytical applications [1, 2]. In recent years, this technique has been extended to deposition of ions onto substrates in ultra-high vacuum (UHV) [3–11]. Electrospray ion beam deposition (ES-IBD) combines ESI further with a quadrupole mass filter and control of the ion–surface collision energy [12–20]. This combination benefits from the broad applicability including many large and fragile molecules, UHV compatibility, mass analysis and filtering, and energy- and dose-control during landing. This results in clean and controlled depositions that are not achievable by sublimation or drop-casting. Control of the landing energy may be achieved by suitable potentials applied to the to the elements guiding the ions into high vacuum [21] or to the sample, as in the present investigations [16]. Deceleration of ions enables so-called soft-landing [13, 22–25] with low translational energies allowing for non-destructive depositions, e.g. no bond cleavage or

conformational changes, of molecules such as transition metal complexes [26], non-sublimable nano ribbons precursors [27, 28] or larger biomolecules [29–31].

Analysis of configurations and conformations of deposited molecules by scanning probe microscopy demonstrates one of its applications, where non-averaging techniques are desired [30–33]. Anggara et al. were able to directly observe the positions of glycan side groups in proteins, which play an important role in the function and dysfunction of various biomolecules [30]. In another study, a cyclic glucose oligomer was deposited, and the positions of hydroxyl groups and intramolecular hydrogen bonds were observed by atomic force microscopy [33]. During the collision with the surface, the molecule's translational energy is redistributed among other degrees of freedom, such as molecular vibrations, on the picosecond timescale [34, 35]. The successful deposition of cytochrome C without major changes in conformation was achieved on freestanding graphene, which acts as a "trampoline" by dissipating the energy away from the protein molecule within a few picoseconds [29].

A controlled increase of the landing energy opens new opportunities for the formation of specific surface species, e.g. via mechanochemistry. The occurrence of these collision-induced changes at higher landing energies is referred to as reactive landing [13, 24, 34–39]. It was shown that non-accessible surface species were observed through controlled C—N bond breaking during landing [35]. The unfolding of the molecular secondary structure, and therefore the conformation of the surface species, is also strongly dependent on the choice of the landing energy [25, 34]. Moreover, fragmentation of molecules can be purposefully employed to form new building blocks for 2D and 3D materials [40]. Therefore, it is important to further investigate the impact of the landing energy of molecules on the occurrence of different surface species or their behaviors.

Here, we investigated a spin-crossover (SCO) active Fe(II) [2 × 2] grid complex (Figure 1a) composed of four ligand **L** molecules (Figure 1b) connected by four Fe(II) ion centers as described by Suryadevara and coworkers [41]. Spin-crossover complexes can undergo a reversible transition between low-spin and high-spin states, a phenomenon governed by factors like temperature, pressure, light exposure, or electric fields making these interesting as molecular electronic/spintronic architectures for applications like data storage, sensors, and actuators [42–49]. The Fe(II) [2 × 2] grid complex is saturated by eight triflate anions ($CF_3SO_3^-$ (OTf^-)).

We deposited the Fe(II) [2 × 2] grid molecules onto an Ag(111) single crystal with different landing energies using a specific ES-IBD system, designated as *electrospray controlled ion beam deposition* (ES-CIBD, Figure 1c) apparatus [16], and imaged the surfaces by scanning tunneling microscopy (STM). At lower landing energies, we observed unordered structures with features of varying sizes. Interestingly, increasing the landing energy resulted in a high variety of well-ordered self-assemblies, which are ascribed to be formed by subunits of the complex (intact ligand **L** and Fe ions) of the Fe(II) [2 × 2] grid complex. Notably, not all well-ordered structures were accessible through the deposition of fragmented Fe(II) [2 × 2] grid complexes or sequential deposition of the **L** and Fe ions, indicating an unexpected influence of ES-CIBD on the formation of different self-assemblies on the Ag(111) surface.

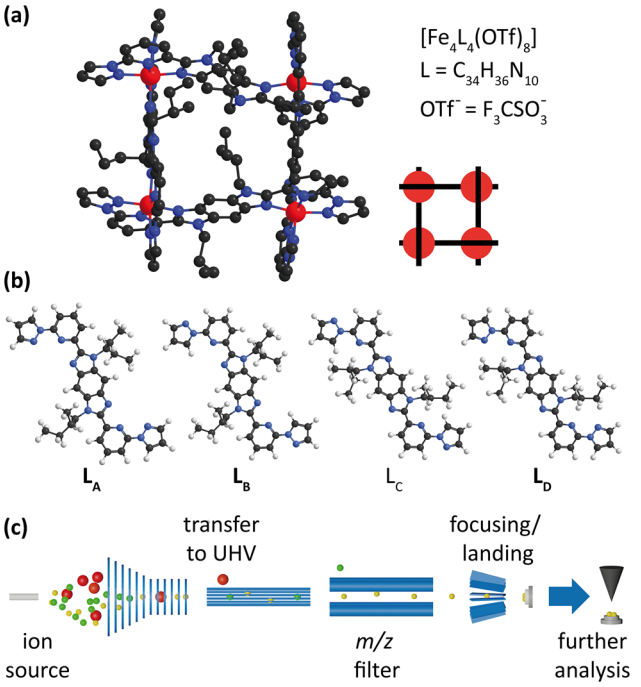

FIGURE 1 | (a) Crystal structure of the Fe(II) [2 × 2] grid complex, $Fe_4(C_{34}H_{36}N_{10})_4(F_3CSO_3)_8$. The hydrogen atoms and counter ions were omitted for clarity. A cartoon representation of the complex is shown next to the molecular structure for clarification, with red circles and black lines representing Fe(II) ions and ligands L ($C_{34}H_{36}N_{10}$), respectively. (b) Rotamers of ligand L: L_A, L_B, L_C, and L_D. N, C, H, and Fe are represented in blue, black, white, and red, respectively. (c) Schematic of the ES-CIBD system.

2 | Results and Discussion

The analysis of the mass spectrum prior deposition of the Fe(II) [2 × 2] grid complex revealed noteworthy peaks at *m/z* values of 475, 584, 601, 611, 789, 1102, and 1728 (Figure 2a). Among these, five peaks can be (at least partially) attributed to the intact $[Fe_4L_4(OTf)_{8-x}]^{x+}$ molecule with the charge states from 2+ to 6+ (Figure 2c). They differ by the number of lost triflate counter anions and consequently by the amount of positive charge of the entire complex and its total mass. The even charge states may also result from fragmentation of the intact complex to $[Fe_2L_2(OTf)_{4-x}]^{x+}$. In contrast, the peaks of odd-numbered charge states can be attributed unambiguously to intact complexes. The peak at *m/z* 611 is ascribed to the molecular fragment $[FeL_2]^{2+}$, whereas the peak with *m/z* 584 is assigned to the protonated ligand $\mathbf{L}H^+$, which is also observable by ES-CIBD of the ligand alone (Figure 2b). For the deposition of an intact complex, the peak at *m/z* 1102 was chosen due to the unambiguity of its composition of solely intact Fe(II) [2 × 2] grid complex ions ($[Fe_4L_4(OTf)_5]^{3+}$) and its low total charge of 3+. For control experiments, $\mathbf{L}H^+$ (Figure 2b) and the fragment of the Fe(II) [2 × 2] grid complex at *m/z* 611 (Figure 2a), exemplifying an already broken complex, were deposited on Ag(111).

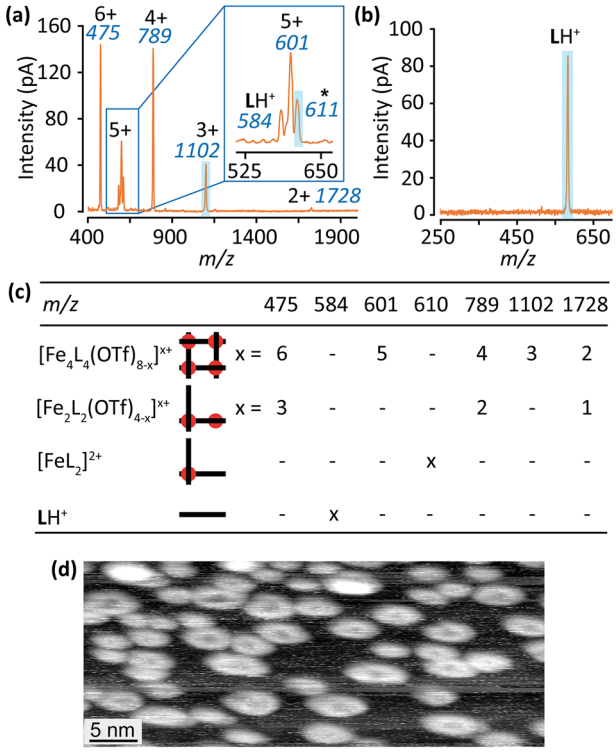

FIGURE 2 | (a) Mass spectra of the Fe(II) [2 × 2] grid complex, with the corresponding charge state of an intact molecule indicated above the respective peaks. The *m/z* values are given in blue italics. The inset provides a zoom-in view with peaks corresponding to $\mathbf{L}H^+$, the intact complex with a charge of 5+, and a fragment of the complex $[FeL_2]$ (*). (b) Mass spectra of protonated ligands **L**. The *m/z* regions used for deposition are indicated in blue in the mass spectra (a) and (b). (c) Summary of all potential species corresponding to the *m/z* peaks in the mass spectrum of the Fe(II) [2 × 2] grid shown in (a). Cartoons illustrate the corresponding intact/molecular fragments of the Fe(II) [2 × 2] grid complex with Fe as red circles and the ligand as black lines. (d) STM image of the deposition of the intact complex (*m/z* 1102) with a mean landing energy of 3 eV z^{-1} (2500 mV, 90 pA, 150 K).

The translational energy distribution of the ions in the beam was acquired by measuring the deposition ion current as a function of the potential applied to the sample [16, 50]. A Gaussian function can be used to describe the distribution (see Figure S1). Adjusting the potential applied to the sample enables controlling the mean landing energy of the deposited species. For this study, mean landing energies per charge (total mean landing energies are given in brackets) of the intact Fe(II) [2 × 2] grid molecule of 1.3 eV z^{-1} (3.9 eV), 3 eV z^{-1} (9 eV), and 24 eV z^{-1} (72 eV) were employed.

Initially, intact Fe(II) [2 × 2] grid ions (*m/z* 1102) were deposited on Ag(111) in the soft-landing regime [13, 22–25] with an average landing energy of 1.3 eV z^{-1}. At 150 K agglomerations of protrusions ranging from 2 to 5 nm in diameter were observed in STM on the Ag(111) surface with submonolayer coverage (see Figure S2). In a second experiment, a higher landing energy of 3 eV z^{-1} was chosen, which also increased the deposition rate. The analysis partially gave rise to similar protrusions already observed for the deposition with lower mean landing energy (see Figure 2d; Figure S2). Astonishingly, additional, well-ordered structures (***α***-***ζ***, see SI for lattice parameters) were found in STM at a sample temperature of 150 K (Figure 3; Table S1). These structures formed islands with dimensions extending well beyond 100 × 100 nm^2 (see Figure S3). With an even higher mean landing energy of 24 eV z^{-1}, which is attributed to reactive landing [13, 24, 36], the round protrusions as shown in Figure 2 were no longer observed. However, the six structures already present with the medium range landing energy were also found after this deposition.

As a control experiment, the protonated ligand $\mathbf{L}H^+$ was deposited by ES-CIBD with an average landing energy of 3 eV z^{-1} (Figure 2b). Protons are assumed to spillover to the Ag(111) surface at room temperature, recombine, and desorb as gaseous H_2 [51–53]. Therefore, it is reasonable to deduce that both the ligand from the complex and the protonated ligand exhibit similar behavior on the surface. The networks ***δ***, ***ε***, and ***ζ*** were recorded by STM at 140 K sample temperature. However, even after adding Fe and annealing the sample to 343 K, structures ***α***, ***β***, and ***γ*** were not observed. Spraying a fragment of the complex (*m/z* 611, $[FeL_2]^{2+}$) with a mean landing energy of 1.6 eV z^{-1} also led only to structures ***δ***, ***ε***, ***ζ***, and unordered areas (see Figure S4). Thus, the structures ***α***, ***β***, and ***γ*** could not be obtained by either of these two experiments. The results of the depositions are summarized in Table 1.

When considering the dimensions of the intact Fe(II) [2 × 2] grid complex, it becomes obvious that ***α***-***ζ*** cannot be substantiated by intact grid molecules. It is therefore essential to consider the single parts of the complex—the ligand **L**, the triflate, and the Fe ions. The triflate anions are most likely too mobile to be participating in the observed structure, and contaminants can be excluded due to the mass selection prior deposition. A fragmentation of the Fe(II) [2 × 2] grid complex can be rationalized, on the one hand, by higher landing energies. For instance, C≡N bond cleavage was reported at 6 eV z^{-1} [35]. Thus, cleavage of the coordination bonds in the Fe(II) [2 × 2] grid complex molecules should be feasible at moderate landing energies. However, even in the soft-landing regime, loss of ligands can be observed due to structural distortions of the metal complexes on the surfaces and charge transfers between substrate and molecules [26].

Importantly, the smallest building blocks of structures ***δ***, ***ε***, and ***ζ*** consist of two neighboring protrusions. Similarly, the structural motifs of ***α***, ***β***, and ***γ*** are based on an even number of protrusions. Moreover, the repeating circular structural element of ***α*** (marked by an orange circle in Figure 3a) can be observed free standing (see Figure S5). The two neighboring protrusions of ***δ***-***ζ*** are spaced 0.75 ± 0.1 nm apart, a distance comparable to that of neighboring protrusions in structures ***α*** to ***γ***. The average distance between the centers of neighboring protrusions aligns with the distance between the centers of two upright isopentanyl side chains of the ligand **L**. This strongly indicates that the two adjacent protrusions correspond to **L**.

Structures ***α*** to ***γ*** share a common motif characterized by six ligands arranged in a circular pattern (Figure 4a–c). In structure ***α***, this motif exists independently, unconnected to other units (Figure 4a). Structure ***β*** features a connection to adjacent circular units, sharing a ligand in one dimension, leading to the formation

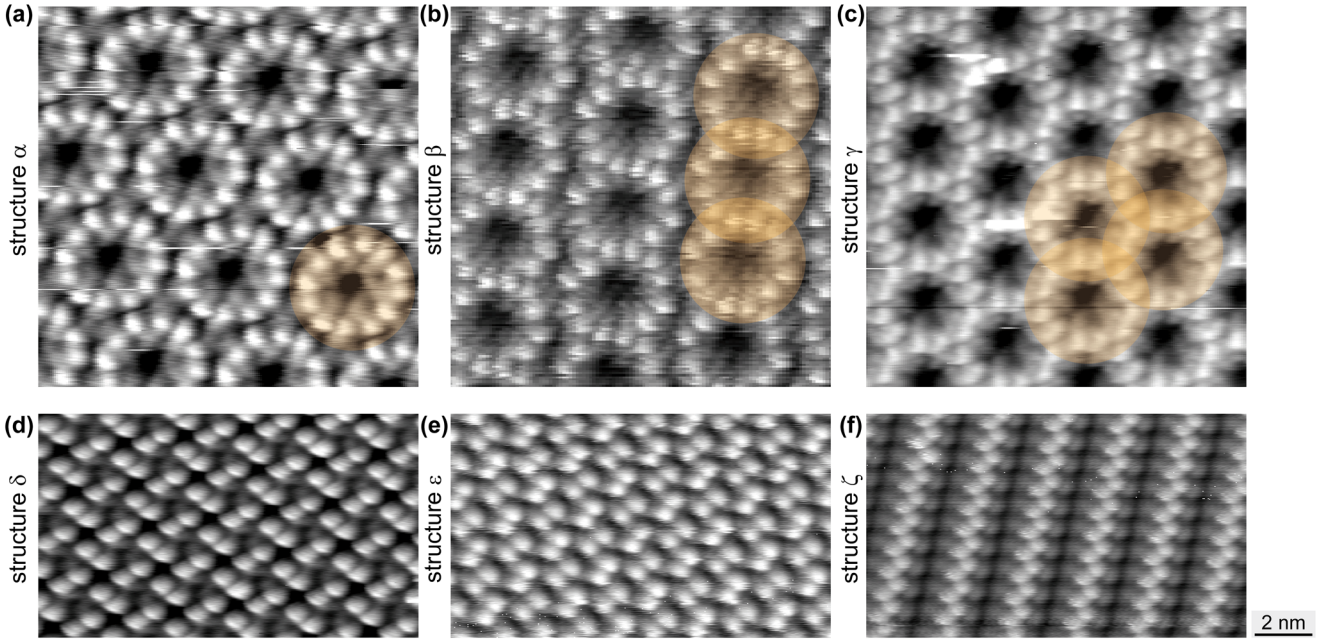

FIGURE 3 | STM images of structures ***α*-*ζ***, which are only observable after depositions of intact Fe grid molecules (*m/z* 1102) with mean landing energy of 3 eV z^{-1} or higher: (a) (2102 mV, 110 pA), (b) (2500 mV, 110 pA), (c) (1768 mV, 90 pA), (d) (2087 mV, 90 pA), (e) (2102 mV, 160 pA) and (f) (1767 mV, 90 pA). All images were taken at 150 K and have the same scale. The orange circles emphasis the 0D, 1D, and 2D structure in a, b, and c, respectively.

TABLE 1 | Summary of deposited species with their respective landing energy and observed surface species by STM.

m/z	Molecular Structure	Mean Landing Energy [eV z^{-1}]	Unordered Structures	*α*-*γ*	*δ*-*ζ*
1102	$[Fe_4L_4(OTf)_5]^{3+}$	< 3	✓	—	—
1102	$[Fe_4L_4(OTf)_5]^{3+}$	> 3	—	✓	✓
611	$[FeL_2]^{2+}$	1.6	✓	—	✓
584	$\mathbf{L}H^+$	3	—	—	✓

of 1D rows (Figure 4b). Structure ***γ*** undergoes a more extensive fusion process in two dimensions, resulting in a well-organized 2D network with a minimal number of irregularities (Figure 4c). Notably, islands of distorted ***δ*** structures border the ***β*** chains, and transitions between ***β*** and ***γ*** are also evident, further illustrating the fusion process of a six-ligand circular motif to a 2D network (see Figure S6).

For the surface structures ***δ***, ***ε***, and ***ζ***, Fe coordination bonds formed on the surface with the ligand can be ruled out as these structures are also observed after the deposition of the ligand without Fe. On the other hand, the presence of ***α***, ***β***, and ***γ*** after the intact Fe grid deposition, but not after solely ligand deposition, makes the presence of Fe in these structures likely. Notably, even the deposition of the complex fragment $[FeL_2]^{2+}$ (*m/z* 611) does not lead to structures ***α***, ***β***, and ***γ***. Hence, it could be that a specific ratio of **L** and Fe is necessary for these structures to form. In the intact complex (*m/z* 1102, 3+), the ratio of Fe to ligand is 1:1. However, in the broken complex fragment *m/z* 611, this ratio shifts to 1:2. Based on these considerations, molecular models were derived for the structures ***α***, ***β*** and ***γ*** consisting of **L** and Fe and for ***δ***, ***ε***, and ***ζ*** consisting of just **L**.

The ligand itself can be found in different surface conformation arising from a rotation about single bonds (Figure 1b). Given the high order and high symmetry of the structures, only symmetric rotamers were considered for deducing the model structures for each self-assembly. We selected the rotamer conformation that best fits the observed contrast in STM and enhances intermolecular interactions through hydrogen bonds and Fe coordination bonds in each network. For the different structures obtained, we propose the models overlaid in Figure 4. Reported N-Fe-coordination bond lengths on Ag(111) range from 1.6 to 2.3 Å and are thus strongly dependent on the geometry of the involved molecules [54–58]. In our models the average distance between N and Fe is 2.5–3.5 Å. Hence, we cannot exclude that the red dots in our models consist of more than one Fe atom [59]. The variety of only **L** containing structures could also be a result of different rotamers on the Ag(111) surfaces.

The observed surface species present only after low and medium landing energy deposition (see Figure S2) cannot be unambiguously assigned to the intact complex. However, we can deduce that the coordination bonds of the Fe(II) [2 × 2] grid molecules are at least partially intact, as none of the structures ***α*-*ζ***, were

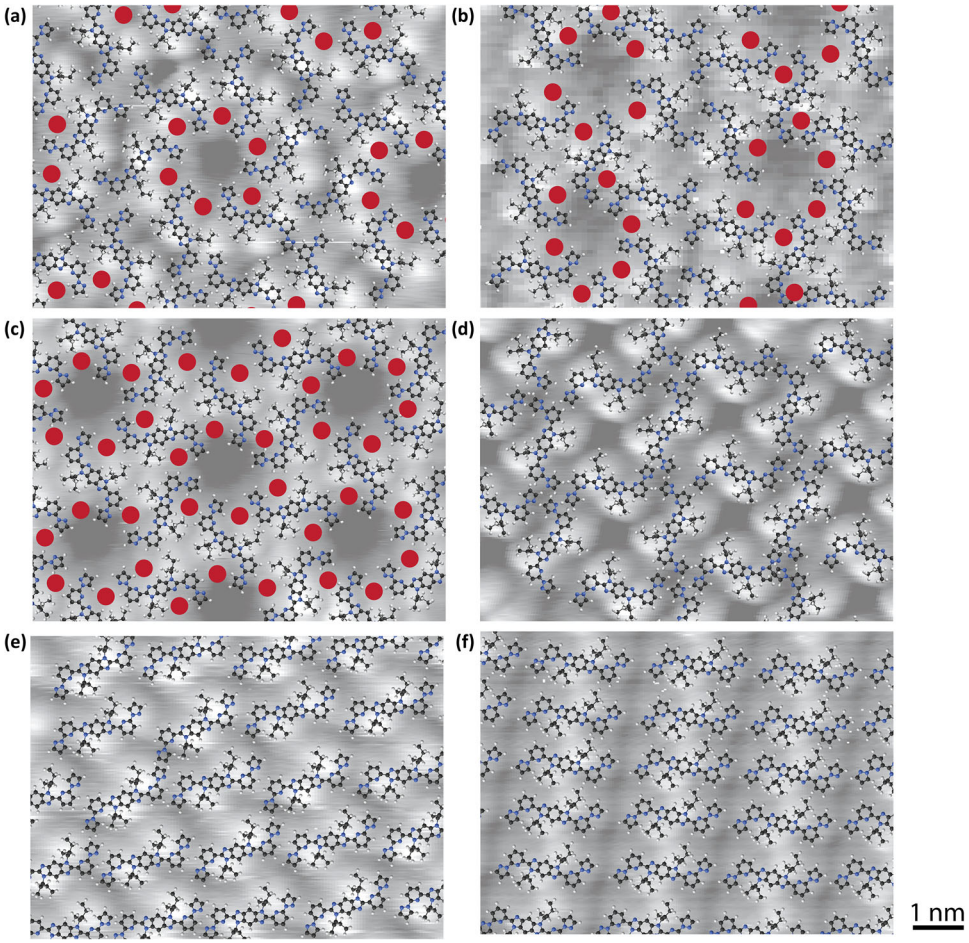

FIGURE 4 | (a–f) Molecular models overlaid to structures α-ζ. N, C, and H atoms are represented in blue, black, and white, respectively. Red circles indicate possible Fe positions.

observed. The variety of sizes observed in STM might be attributed to different landing geometries [34, 35] and hence different interactions with the substrate [26].

3 | Conclusion

In summary, an Fe(II) [2 × 2] grid complex was deposited onto the Ag(111) substrate using ES-IBD. Depending on the mean landing energy, structures of potentially intact Fe(II) [2 × 2] grid complexes and/or a variety of self-assemblies, resulting from the complete fragmentation of coordination bonds in the Fe(II) [2 × 2] grid complexes, were observed on the surface. Among the obtained self-assemblies, three could only be attainable through medium to high energy deposition of the intact complex. These featured novel, planar coordination structures of 0D, 1D, and 2D character. The remaining structures could be consistently replicated by depositing uncoordinated ligands. Even the deposition of a fragment of the complex (m/z 611) could not reproduce all surface structures observed after the deposition of the intact Fe(II) [2 × 2] grid. This underscores the capability of ES-IBD to produce structures that are challenging to achieve through the deposition of individual building blocks alone. Therefore, further research of landing energy dependent self-assembly structures seems worthwhile. The present study represents an initial step and promising insights toward a wider range of tailored surface structure formations. Protocols integrating additional parameters such as the metal-to-ligand ratio or charge balance, which was already shown to control surface structure and composition [21, 60], remains to be explored.

4 | Experimental Methods

4.1 | Electrospray ion beam deposition (ES-IBD)

The Fe grid was solved in acetonitrile (c = 10^{-5} to 10^{-4} mol/l). The ligand was solved in acetonitrile (c = 10^{-4} mol/l) with 1% acetic acid. A fused silica capillary with inner and outer diameters of 0.075 and 0.360 mm, respectively, was used as the ESI emitter. The ESI source was operated in positive mode with an applied voltage of 2.5 to 3 kV. to the emitter. In general, lower emitter voltages and lower molecule charge aid the preservation of the conformation of electrosprayed molecules and, for proteins and nucleic acids, result in conformations closer to their native states [61]. In contrast, in our case positive mode was selected due to the high charge state of the Fe(II) grid (8+) and the weakly bound triflate counterions [41, 62]. The resulting mass spectra showed efficient electrospray ionization. The electrospray voltage of the emitter was optimized by maximizing and stabilizing the deposition current at the sample. The inlet to the UHV system is based on the design by Rauschenbach et al. [63]. and was heated

to 350 K during deposition. The exact geometries and a detailed discussion of the ESI setup and the ion guides along the ion beam can be found elsewhere [16]. A digital quadrupole mass filter was used to analyze the ion beam and ensure the selective deposition of a single molecular species. Prior to each deposition, a mass spectrum was acquired to verify the composition of the ion beam. The translational energy distribution of the ions was determined by measuring the deposition current as a function of cut-off energy [16]. The landing energy was controlled by suitable potentials applied to the sample [16]. The deposition was performed in a UHV chamber with a base pressure of 5×10^{-10} mbar. No pressure increase during deposition was observed.

4.2 | Scanning tunneling microscopy (STM)

The ES-CIBD system is connected to a UHV system consisting of a preparation and an analysis chamber, with a base pressure of below 2×10^{-10} mbar in each. The Ag(111) crystal was prepared in the preparation chamber prior to ES-IBD by a sequence of rt Ar^+ sputtering followed by an anneal to 700 K. The analysis chamber is equipped with an Aarhus-type STM from Specs GmbH with a chemically etched tungsten tip. Following the bakeout of the analysis chamber to achieve UHV conditions, the tip was sputtered in situ by Ar^+ ions. The STM cradle with the sample was pre-cooled with LN_2, while the STM scanner was counter heated to 273 K, so as to maintain the calibration parameters of the piezoelectric elements positioning the tip. The tunneling bias is applied to the sample. The tunneling conditions and acquisition temperatures of STM images are reported in the respective Figure caption.

Acknowledgments

Open access funding enabled and organized by Projekt DEAL.

Funding

We acknowledge the financial support received from the German Research Foundation (DFG) under the priority program COORNETs (SPP1928/project number 316890188) and the e-conversion Cluster of Excellence (project number 390776260). Additionally, we express our appreciation for the funding provided by the German Federal Ministry of Economic Affairs and Climate Action through the EXIST-Forschungstransfer program.

Conflicts of Interest

Andreas Walz, Annette Huettig, and Hartmut Schlichting are currently employees of pureions GmbH, manufacturer for ES-CIBD devices and digital quadrupole mass spectrometers (dQMFs), that base on the technology of the instrument used in this publication. No further conflicts are to declare.

Data Availability Statement

The data that support the findings of this study are available from the corresponding author upon reasonable request.

References

1. J. B. Fenn, M. Mann, C. K. Meng, S. F. Wong, and C. M. Whitehouse, "Electrospray Ionization for Mass Spectrometry of Large Biomolecules," *Science* 246, no. 4926 (1989): 64–71, https://doi.org/10.1126/science.2675315.

2. J. B. Fenn, "Electrospray Wings for Molecular Elephants (Nobel Lecture)," *Angewandte Chemie International Edition* 42, no. 33 (2003): 3871–3894, https://doi.org/10.1002/anie.200300605.

3. J. C. Swarbrick, J. B. Taylor, and J. N. O'Shea, "Electrospray Deposition in Vacuum," *Applied Surface Science* 252, no. 15 (2006): 5622–5626, https://doi.org/10.1016/j.apsusc.2005.12.025.

4. C. J. Satterley, L. M. A. Perdigão, A. Saywell, et al., "Electrospray Deposition of Fullerenes in Ultra-High Vacuum: In Situ Scanning Tunneling Microscopy and Photoemission Spectroscopy," *Nanotechnology* 18, no. 45 (2007): 455304, https://doi.org/10.1088/0957-4484/18/45/455304.

5. A. Hinaut, R. Pawlak, E. Meyer, and T. Glatzel, "Electrospray Deposition of Organic Molecules on Bulk Insulator Surfaces," *Beilstein Journal of Nanotechnology* 6 (2015): 1927–1934, https://doi.org/10.3762/bjnano.6.195.

6. C. J. Judd, D. V. Kondratuk, H. L. Anderson, and A. Saywell, "On-Surface Synthesis Within a Porphyrin Nanoring Template," *Scientific Reports* 9, no. 1 (2019): 9352, https://doi.org/10.1038/s41598-019-45359-w.

7. R. Pawlak, J. G. Vilhena, A. Hinaut, et al., "Conformations and Cryo-Force Spectroscopy of Spray-Deposited Single-Strand DNA on Gold," *Nature Communications* 10, no. 1 (2019): 685, https://doi.org/10.1038/s41467-019-08531-4.

8. S. Scherb, A. Hinaut, R. Pawlak, et al., "Giant Thermal Expansion of a Two-Dimensional Supramolecular Network Triggered by Alkyl Chain Motion," *Communications Materials* 1, no. 1 (2020): 8, https://doi.org/10.1038/s43246-020-0009-2.

9. C. Méthivier, P. Cornette, D. Costa, and J. Landoulsi, "Electrospray Ion Beam Deposition of Small Peptides on Solid Surfaces: A Molecular Level Description of the Glutathione/Copper Interface," *Applied Surface Science* 612 (2023): 155895, https://doi.org/10.1016/j.apsusc.2022.155895.

10. J. Lê-Chesnais, M. Steffenhagen, C. Méthivier, et al., "Binding Mechanism of Oligopeptides on Solid Surface: Assessing the Significance of Single-Molecule Approach," *Nanoscale* 17, no. 6 (2025): 3460–3477, https://doi.org/10.1039/D4NR04474F.

11. K. Kolar, M. Kappe, H. Siboni, et al., "Clean Electrospray Deposition of Porphyrin Molecules and Polyethylene Glycol Chains onto a Au(100) Surface," *The Journal of Physical Chemistry C* 130, no. 1 (2026): 650–660, https://doi.org/10.1021/acs.jpcc.5c06482.

12. S. Rauschenbach, F. L. Stadler, E. Lunedei, et al., "Electrospray Ion Beam Deposition of Clusters and Biomolecules," *Small* 2, no. 4 (2006): 540–547, https://doi.org/10.1002/smll.200500479.

13. S. Rauschenbach, R. Vogelgesang, N. Malinowski, et al., "Electrospray Ion Beam Deposition: Soft-Landing and Fragmentation of Functional Molecules at Solid Surfaces," *ACS Nano* 3, no. 10 (2009): 2901–2910, https://doi.org/10.1021/nn900022p.

14. C. Hamann, R. Woltmann, I.-P. Hong, N. Hauptmann, S. Karan, and R. Berndt, "Ultrahigh Vacuum Deposition of Organic Molecules by Electrospray Ionization," *Review of Scientific Instruments* 82, no. 3 (2011): 033903, https://doi.org/10.1063/1.3553010.

15. K. D. D. Gunaratne, V. Prabhakaran, Y. M. Ibrahim, R. V. Norheim, G. E. Johnson, and J. Laskin, "Design and Performance of a High-Flux Electrospray Ionization Source for Ion Soft Landing," *The Analyst* 140, no. 9 (2015): 2957–2963, https://doi.org/10.1039/C5AN00220F.

16. A. Walz, K. Stoiber, A. Huettig, H. Schlichting, and J. V. Barth, "Navigate Flying Molecular Elephants Safely to the Ground: Mass-Selective Soft Landing up to the Mega-Dalton Range by Electrospray Controlled Ion-Beam Deposition," *Analytical Chemistry* 94, no. 22 (2022): 7767–7778, https://doi.org/10.1021/acs.analchem.1c04495.

17. J. Laskin, P. Wang, and O. Hadjar, "Soft-Landing of Peptide Ions Onto Self-Assembled Monolayer Surfaces: An Overview," *Physical Chemistry Chemical Physics* 10, no. 8 (2008): 1079–1090, https://doi.org/10.1039/B712710C.

18. S. Rauschenbach, M. Ternes, L. Harnau, and K. Kern, "Mass Spectrometry as a Preparative Tool for the Surface Science of Large Molecules," *Annual Review of Analytical Chemistry* 9, no. 1 (2016): 473–498, https://doi.org/10.1146/annurev-anchem-071015-041633.

19. L. Eriksson, T. K. Esser, M. Grabarics, et al., "High-Resolution CryoEM Structure Determination of Soluble Proteins After Soft-Landing ESIBD," *arXiv* (2025): 250322364, https://doi.org/10.48550/arXiv.2503.22364.

20. A. Hinaut, S. Scherb, X. Yao, et al., "Stable Au(111) Hexagonal Reconstruction Induced by Perchlorinated Nanographene Molecules," *The Journal of Physical Chemistry C* 128 (2024): 18894–18900, https://doi.org/10.1021/acs.jpcc.4c03812.

21. H. Y. Samayoa-Oviedo, K.-A. Behrend, S. Kawa, et al., "Design and Performance of a Soft-Landing Instrument for Fragment Ion Deposition," *Analytical Chemistry* 93, no. 43 (2021): 14489–14496, https://doi.org/10.1021/acs.analchem.1c03009.

22. W.-P. Peng, G. E. Johnson, I. C. Fortmeyer, et al., "Redox Chemistry in Thin Layers of Organometallic Complexes Prepared Using Ion Soft Landing," *Physical Chemistry Chemical Physics* 13, no. 1 (2011): 267–275, https://doi.org/10.1039/C0CP01457E.

23. J. Laskin, G. E. Johnson, J. Warneke, and V. Prabhakaran, "From Isolated Ions to Multilayer Functional Materials Using Ion Soft Landing," *Angewandte Chemie International Edition* 57, no. 50 (2018): 16270–16284, https://doi.org/10.1002/anie.201712296.

24. G. Verbeck, W. Hoffmann, and B. Walton, "Soft-Landing Preparative Mass Spectrometry," *The Analyst* 137, no. 19 (2012): 4393–4407, https://doi.org/10.1039/C2AN35550G.

25. D. Meier, B. Schoof, J. Wang, et al., "Structural Adaptations of Electrosprayed Aromatic Oligoamide Foldamers on Ag(111)," *Chemical Communications* 58, no. 64 (2022): 8938–8941, https://doi.org/10.1039/D2CC03286D.

26. H. Y. Samayoa-Oviedo, H. Knorke, J. Warneke, and J. Laskin, "Spontaneous Ligand Loss by Soft Landed $[Ni(bpy)_3]^{2+}$ Ions on Perfluorinated Self-Assembled Monolayer Surfaces," *Chemical Science* 15, no. 28 (2024): 10770–10783, https://doi.org/10.1039/D4SC02527J.

27. W. Ran, A. Walz, K. Stoiber, et al., "Depositing Molecular Graphene Nanoribbons on Ag(111) by Electrospray Controlled Ion Beam Deposition: Self-Assembly and On-Surface Transformations," *Angewandte Chemie International Edition* 14, no. 61 (2022): 202111816, https://doi.org/10.1002/anie.202111816.

28. X. Zhang, V. Srot, X. Wu, et al., "Controlled Formation of Nanoribbons and Their Heterostructures via Assembly of Mass-Selected Inorganic Ions," *Advanced Materials* 36, no. 23 (2024): 2310817, https://doi.org/10.1002/adma.202310817.

29. K. Anggara, H. Ochner, S. Szilagyi, L. Malavolti, S. Rauschenbach, and K. Kern, "Landing Proteins on Graphene Trampoline Preserves Their Gas-Phase Folding on the Surface," *ACS Central Science* 9, no. 2 (2023): 151–158, https://doi.org/10.1021/acscentsci.2c00815.

30. K. Anggara, L. Srsan, T. Jaroentomeechai, et al., "Direct Observation of Glycans Bonded to Proteins and Lipids at the Single-Molecule Level," *Science* 382, no. 6667 (2023): 219–223, https://doi.org/10.1126/science.adh3856.

31. J. Seibel, K. Anggara, M. Delbianco, and S. Rauschenbach, "Scanning Probe Microscopy Characterization of Biomolecules enabled by Mass-Selective, Soft-landing Electrospray Ion Beam Deposition," *ChemPhysChem* 25, no. 21 (2024): 202400419, https://doi.org/10.1002/cphc.202400419.

32. X. Wu, M. Delbianco, K. Anggara, et al., "Imaging Single Glycans," *Nature* 582, no. 7812 (2020): 375–378, https://doi.org/10.1038/s41586-020-2362-1.

33. M. Grabarics, B. Mallada, S. Edalatmanesh, et al., "Atomically Resolved Imaging of the Conformations and Adsorption Geometries of Individual β-Cyclodextrins With Non-Contact AFM," *Nature Communications* 15, no. 1 (2024): 9482, https://doi.org/10.1038/s41467-024-53555-0.

34. K. Anggara, Y. Zhu, M. Delbianco, et al., "Exploring the Molecular Conformation Space by Soft Molecule–Surface Collision," *Journal of the American Chemical Society* 142, no. 51 (2020): 21420–21427, https://doi.org/10.1021/jacs.0c09933.

35. L. Krumbein, K. Anggara, M. Stella, et al., "Fast Molecular Compression by a Hyperthermal Collision Gives Bond-Selective Mechanochemistry," *Physical Review Letters* 126, no. 5 (2021): 056001, https://doi.org/10.1103/PhysRevLett.126.056001.

36. G. E. Johnson and J. Laskin, "Preparation of Surface Organometallic Catalysts by Gas-Phase Ligand Stripping and Reactive Landing of Mass-Selected Ions," *Chemistry – A European Journal* 16, no. 48 (2010): 14433–14438, https://doi.org/10.1002/chem.201002292.

37. P. Wang and J. Laskin, "Helical Peptide Arrays on Self-Assembled Monolayer Surfaces Through Soft and Reactive Landing of Mass-Selected Ions," *Angewandte Chemie International Edition* 47, no. 35 (2008): 6678–6680, https://doi.org/10.1002/anie.200801366.

38. N. Hauptmann, C. Hamann, H. Tang, and R. Berndt, "Soft-Landing Electrospray Deposition of the Ruthenium Dye N3 on Au(111)," *The Journal of Physical Chemistry C* 117, no. 19 (2013): 9734–9738, https://doi.org/10.1021/jp311420d.

39. T. Knaak, C. González, Y. J. Dappe, et al., "Fragmentation and Distortion of Terpyridine-Based Spin-Crossover Complexes on Au(111)," *The Journal of Physical Chemistry C* 123, no. 7 (2019): 4178–4185, https://doi.org/10.1021/acs.jpcc.8b11242.

40. J. Warneke, H. Y. Samayoa-Oviedo, M. Rohdenburg, X. Li, H. Knorke, and J. Laskin, "Molecular Synthesis With Gaseous Fragment Ions on Surfaces," *Nature Reviews Chemistry* 9, no. 7 (2025): 470–480, https://doi.org/10.1038/s41570-025-00719-1.

41. N. Suryadevara, A. Pausch, E. Moreno-Pineda, et al., "Chiral Resolution of Spin-Crossover Active Iron(II) [2×2] Grid Complexes," *Chemistry – A European Journal* 27, no. 61 (2021): 15172–15180, https://doi.org/10.1002/chem.202101432.

42. O. Kahn, J. Kröber, and C. Jay, "Spin Transition Molecular Materials for Displays and Data Recording," *Advanced Materials* 4, no. 11 (1992): 718–728, https://doi.org/10.1002/adma.19920041103.

43. R. Chandrasekar, F. Schramm, O. Fuhr, and M. Ruben, "An Iron(II) Spin-Transition Compound With Thiol Anchoring Groups," *European Journal of Inorganic Chemistry* 2008 (2008): 2649–2653, https://doi.org/10.1002/ejic.200800212.

44. K. S. Kumar and M. Ruben, "Emerging Trends in Spin Crossover (SCO) Based Functional Materials and Devices," *Coordination Chemistry Reviews* 346 (2017): 176–205, https://doi.org/10.1016/j.ccr.2017.03.024.

45. K. S. Kumar, I. Šalitroš, Z. Boubegtiten-Fezoua, S. Moldovan, P. Hellwig, M. Ruben, et al., "A Spin Crossover (SCO) Active Graphene-Iron(II) Complex Hybrid Material," *Dalton Transactions* 47, no. 1 (2018): 35–40, https://doi.org/10.1039/C7DT03623J.

46. M. Gruber and R. Berndt, "Spin-Crossover Complexes in Direct Contact With Surfaces," *Magnetochemistry* 6, no. 3 (2020): 35, https://doi.org/10.3390/magnetochemistry6030035.

47. S. Johannsen, S. Ossinger, T. Markussen, F. Tuczek, M. Gruber, and R. Berndt, "Electron-Induced Spin-Crossover in Self-Assembled Tetramers," *ACS Nano* 15, no. 7 (2021): 11770–11778, https://doi.org/10.1021/acsnano.1c02698.

48. S. Johannsen, S. Ossinger, J. Grunwald, et al., "Spin Crossover in a Cobalt Complex on Ag(111)," *Angewandte Chemie International Edition* 61, no. 12 (2022): 202115892, https://doi.org/10.1002/anie.202115892.

49. S. Johannsen, S. Schüddekopf, S. Ossinger, et al., "Three-State Switching of an Fe Spin Crossover Complex," *The Journal of Physical Chemistry C* 126, no. 16 (2022): 7238–7244, https://doi.org/10.1021/acs.jpcc.2c00473.

50. S. Zhang, D. Meier, P. Lawes, et al., "Landing-Energy-Controlled Surface Conformation of Electrosprayed Foldamer Molecules on Au(111),"

ACS Nano 20, no. 4 (2026): 3402–3409, https://doi.org/10.1021/acsnano.5c12973.

51. G. Lee, P. T. Sprunger, M. Okada, D. B. Poker, D. M. Zehner, and E. W. Plummer, "Chemisorption of Hydrogen on the Ag(111) Surface," *Journal of Vacuum Science & Technology A: Vacuum, Surfaces, and Films* 12, no. 4 (1994): 2119–2123, https://doi.org/10.1116/1.579147.

52. M. Röckert, M. Franke, Q. Tariq, et al., "Insights in Reaction Mechanistics: Isotopic Exchange during the Metalation of Deuterated Tetraphenyl-21,23*D*-Porphyrin on Cu(111)," *Journal of Physical Chemistry C* 118, no. 46 (2014): 26729–26736, https://doi.org/10.1021/jp507303h.

53. S. Massicot, T. Sasaki, M. Lexow, et al., "Adsorption, Wetting, Growth, and Thermal Stability of the Protic Ionic Liquid Diethylmethylammonium Trifluoromethanesulfonate on Ag(111) and Au(111)," *Langmuir* 37, no. 39 (2021): 11552–11560, https://doi.org/10.1021/acs.langmuir.1c01823.

54. Z. Shi and N. Lin, "Structural and Chemical Control in Assembly of Multicomponent Metal−Organic Coordination Networks on a Surface," *Journal of the American Chemical Society* 132, no. 31 (2010): 10756–10761, https://doi.org/10.1021/ja1018578.

55. T. Lin, G. Kuang, X. S. Shang, P. N. Liu, and N. Lin, "Self-assembly of Metal–organic Coordination Networks using On-Surface Synthesized Ligands," *Chemical Communications* 50, no. 97 (2014): 15327–15329, https://doi.org/10.1039/C4CC07604D.

56. P. Knecht, N. Suryadevara, B. Zhang, et al., "The Self-Assembly and Metal Adatom Coordination of a Linear Bis-Tetrazole Ligand on Ag(111)," *Chemical Communications* 54, no. 72 (2018): 10072–10075, https://doi.org/10.1039/C8CC04323J.

57. H. Xu, R. Chakraborty, A. K. Adak, et al., "On-Surface Isomerization of Indigo Within 1D Coordination Polymers," *Angewandte Chemie International Edition* 63, no. 15 (2024): 202319162, https://doi.org/10.1002/anie.202319162.

58. H. Xu, R. Chakraborty, B. Yang, et al., "On-Surface Indigo-Based Bimolecular Coordination Networks With Programmable Regular or Vitreous Structure," *Advanced Functional Materials* (2025): 12253, https://doi.org/10.1002/adfm.202512253.

59. C. Krull, M. Castelli, P. Hapala, et al., "Iron-Based Trinuclear Metal-Organic Nanostructures on a Surface With Local Charge Accumulation," *Nature Communications* 9, no. 1 (2018): 3211, https://doi.org/10.1038/s41467-018-05543-4.

60. F. Yang, K. A. Behrend, H. Knorke, et al., "Anion–Anion Chemistry With Mass-Selected Molecular Fragments on Surfaces," *Angewandte Chemie International Edition* 60, no. 47 (2021): 24910–24914, https://doi.org/10.1002/anie.202109249.

61. L. M. Miller, B. E. Draper, L. F. Barnes, P. C. Ofoegbu, and M. F. Jarrold, "Analysis of Megadalton-Sized DNA by Charge Detection Mass Spectrometry: Entropic Trapping and Shearing in Nanoelectrospray," *Analytical Chemistry* 95, no. 23 (2023): 8965–8973, https://doi.org/10.1021/acs.analchem.3c01027.

62. B. Schäfer, J.-F. Greisch, I. Faus, et al., "Divergent Coordination Chemistry: Parallel Synthesis of [2×2] Iron(II) Grid-Complex Tauto-Conformers," *Angewandte Chemie International Edition* 55, no. 36 (2016): 10881–10885, https://doi.org/10.1002/anie.201603916.

63. M. Pauly, M. Sroka, J. Reiss, et al., "A Hydrodynamically Optimized Nano-Electrospray Ionization Source and Vacuum Interface," *The Analyst* 139, no. 8 (2014): 1856–1867, https://doi.org/10.1039/C3AN01836A.

Supporting Information

Additional supporting information can be found online in the Supporting Information section.

Supporting File: smtd70536-sup-0001-SuppMat.docx.